Analyst

ROYAL SOCIETY OF CHEMISTRY

PAPER

View Article Online
View Journal | View Issue

Cite this: *Analyst*, 2024, **149**, 2034

Improving design features and air bubble manipulation techniques for a single-step sandwich electrochemical ELISA incorporating commercial electrodes into capillary-flow driven immunoassay devices†

Phuritat Kaewarsa, [a] Melissa S. Schenkel,[b] Kira L. Rahn,[b] Wanida Laiwattanapaisal [c] and Charles S. Henry *[b,d]

Integrating electrochemistry into capillary-flow driven immunoassay devices provides unique opportunities for quantitative point-of-care testing. Although custom electrodes can be inexpensive and are tunable, they require skilled fabrication. Here, we report the incorporation of a commercial electrode into a capillary-flow driven immunoassay (iceCaDI) device for a single end-user step sandwich electrochemical enzyme-linked immunosorbent assay (ELISA). The iceCaDI device is a pump-free portable microfluidic device with an integrated commercial screen-printed electrode and flow driven by capillary action. The iceCaDI device is composed of alternating polyester transparency film and double-sided adhesive film layers that are patterned with a laser cutter. This platform was designed to address known limitations of laminated device fabrication methods and operation. First, we developed a foldable laminated device fabrication using hinges for easy assembly and precise alignment. Second, reagent dispersing was achieved by incorporating a 1 mm wide arrow-shaped notch in the middle of the channel that trapped an air bubble and formed a baffle that facilitated reagent spreading to cover the detection area. Third, small vent holes were added to the top layer of the channels to prevent air bubbles from blocking flow. Finally, we fabricated a CRP immunosensor with a detection range of 0.625 to 10.0 μg mL^{-1} as a proof-of-concept to demonstrate an automatically driven sandwich electrochemical ELISA using the iceCaDI device. Three concentrations of CRP were successfully measured under flow conditions within 8 min. Our proposed device is a promising approach and a step forward in the development of point-of-care (POC) devices for techniques that traditionally require multiple user steps.

Received 6th October 2023,
Accepted 15th February 2024

DOI: 10.1039/d3an01704d

rsc.li/analyst

1. Introduction

Point-of-care testing (POCT) allows diagnostics to be performed outside of a centralized laboratory setting and serves as an important tool to facilitate healthcare access for a variety of outcomes such as early diagnosis,[1] therapeutic decisions,[2] and monitoring of disease progression.[3,4] Trends in POCT development aim to improve upon the REASSURED criteria, which stands for real-time connectivity, ease of specimen collection, affordable, sensitive, specific, user-friendly, rapid & robust, equipment-free, and deliverable to end users.[5,6] Although a variety of tests for clinical markers are currently available commercially, there is consistently a need to develop innovative methods to provide faster, cheaper, and quantitative results in POCT settings.

Lateral flow assays (LFAs) have been widely utilized as POC tests, initially for at-home pregnancy tests and most recently for SARS-CoV-2 antigen detection.[7–9] LFAs rely on the capture of the antigen by a selective capture probe, often an antibody, which is coated on a nitrocellulose membrane, followed by binding of a detector probe, such as an antibody conjugated with a gold nanoparticle. These immunoassays generate

[a]*Graduate Program in Clinical Biochemistry and Molecular Medicine, Department of Clinical Chemistry, Faculty of Allied Health Sciences, Chulalongkorn University, Bangkok, 10330, Thailand*
[b]*Department of Chemistry, Colorado State, University, Fort Collins, Colorado, 80526, USA*
[c]*Biosensors and Bioanalytical Technology for Cell and Innovative Testing Research Unit, Department of Clinical Chemistry, Faculty of Allied Health Sciences, Chulalongkorn University, Bangkok, 10330, Thailand*
[d]*Materials and Metallurgy Research Institute, Chulalongkorn University, Bangkok, 10330, Thailand. E-mail: chuck.henry@colostate.edu*
† Electronic supplementary information (ESI) available. See DOI: https://doi.org/10.1039/d3an01704d

qualitative and semi-quantitative results. Unlike traditional enzyme-linked immunosorbent assays (ELISAs), LFAs greatly reduce complicated steps, eliminate the need for sophisticated instruments, and are portable, disposable, and easy to use by untrained personnel.[10] The main disadvantages of LFAs are the use of gold nanoparticle-labelled detector probes that do not amplify the signal like enzyme-labelled detector probes, and the lack of washing steps to decrease non-specific signals. The sensitivity of enzymatic assays is 10–30 times higher than single-reporter systems (like traditional LFAs) because each enzyme generates several reporter molecules.[11–14] In addition, non-specific binding in nitrocellulose is a challenge that requires lengthy optimization to overcome.[15–18] Furthermore, sample evaporation can occur due to slow flow rates obtained in nitrocellulose, and the changes caused by swelling after the membrane is wetted can cause unexpected flow changes.[19–21] Therefore, alternative approaches have been sought to improve POC tests.

Our group recently miniaturized ELISAs using a capillary-flow driven microfluidic device that automates sequential reagent delivery and washing steps.[22,23] Laminated capillary-driven microfluidic devices are attractive platforms for POC tests because of their low cost and small size.[24] This microfluidic system is composed of at least three layers, including top and bottom layers that sandwich a double-sided adhesive (DSA) middle layer that has a cut-out of the channel design. The solution in the closed channel is transported to the outlet by capillary force.[25] These microfluidic devices are advantageous because they do not require an external pump, the solution flow is fast and uniform, and there is less non-specific adsorption than in purely paper-based microfluidic devices. However, several challenges persist in these devices, for example, air bubbles can be trapped within the channel when the solution flows from both directions, stopping fluid flow. Additionally, reagent dispersing can be difficult to facilitate in these devices and obtaining precise alignment of multiple layers to fabricate the device is challenging.

While multiple forms of detection are available for capillary-flow microfluidic devices, electrochemical detection is particularly attractive because sensitive and quantitative results can be obtained using low-cost and portable instrumentation.[26–30] In our previous publications with electrochemical capillary-flow microfluidic devices, we have fabricated screen-printed electrodes in-house because they are low cost, have tunable designs, and can be printed directly on the top layer of the microfluidic device.[22,31] However, in-house electrodes require specialized materials, added time, and specialized skills and tools for fabrication.[32–34] In contrast, commercial electrodes are more reliable, reproducible, and precise.[35–37] Here, we demonstrate a single user-step electrochemical ELISA (eELISA) for C-reactive protein (CRP) by incorporating commercial electrodes into a laminated capillary-driven microfluidic device.

CRP, which is correlated with systemic inflammation, has been identified as a sensitive biomarker for monitoring tissue inflammation, infection progression, tumor stage, and treatment outcomes in humans for conditions such as sepsis, rheumatoid arthritis, systemic lupus erythematosus (SLE), cardiovascular disease, diabetes, malaria, cancer, burns, and post-surgery recovery.[38–40] Thus, monitoring CRP levels is important and a fast, inexpensive, and accessible test would be useful. Immunoassays are typically used for CRP measurements. Advancements in immunosensing techniques for CRP measurement have included label-free detection using electrochemical impedance spectroscopy (EIS),[41] and LFAs using quantum dots[42] and nanoparticles,[43] among others. Although several quantitative CRP tests have been developed, none of them were successfully implemented as POCT due to the need for the complex user-steps or expensive instrumentation.

In this work, we describe the incorporation of commercial electrodes into a capillary-driven immunoassay (iceCaDI) device for single-user step CRP quantification. We create a chamber in the microfluidic device to integrate a commercial electrode. As a proof-of-concept of the new device, CRP levels are quantified in one step by sandwich eELISA, where the enzyme label, horseradish peroxidase, catalyzes the oxidation of TMB (3,3′,5,5′-tetramethylbenzidine), which is subsequently quantified using a reduction potential and chronoamperometry. Furthermore, we describe an easier fabrication technique for multi-layer devices by adding a hinge to guide folding of the layers for precise alignment. We are also the first to report air bubble manipulation in laminated devices, both by trapping an air bubble in a controlled location to facilitate spreading flow over electrodes and by eliminating trapped air bubbles that lead to undesirable stopped flow in the microfluidic device by incorporating vent holes. Therefore, our improved device design has a major impact on the prospects for capillary-driven microfluidic device development.

2. Experimental

2.1 Chemicals and materials

The CRP Protein (>95%, 30-AC05AF), and detector CRP antibodies (10c-CR2015M) were purchased from Fitzgerald (MA, USA). The detector CRP antibody was modified using a horseradish peroxidase (HRP) Conjugation Kit – Lightning-Link® manufacturer (ab102890, Abcam, UK). A biotinylated CRP capture antibody (MAB5101) was ordered from Abnova (Taiwan). Biotinylated HRP was purchased from Invitrogen™ (MA, USA). MES, potassium chloride (KCl), 1-ethyl-3-(3-dimethylaminopropyl) carbodiimide (EDC), 3-pyridinepropionic acid (PPA), TMB (T0440), potassium hexacyanoferrate(II) trihydrate, potassium ferricyanide(III) trihydrate, Tris-HCl, thimerosal, sodium hydroxide (NaOH), phosphate buffered saline (PBS) tablets, sodium tetraborate, and streptavidin were purchased from Sigma-Aldrich (MO, USA). Boric acid, bovine serum albumin (BSA), casein, *N*-hydroxysuccinimide (NHS), sucrose, tween 20, and tween 80 were purchased from Thermo Fisher Scientific (MA, USA). All solutions were prepared by ultrapure water (18.2 MΩ cm) purified at 25 °C using a Milli-Q system (MilliporeSigma, MA, USA).

Transparency film (9984: Polyethylene terephthalate (PET) sheet) and double-sided adhesive film (DSA: 467MP and 468MP) were purchased from 3M (MN, USA). Unmodified glass fibers with PVA binder were purchased from MilliporeSigma (Burlington, MA). Whatman No. 4 filter paper was purchased from GE Healthcare Sciences (England). Carbon (DRP-110-U75) and other screen-printed electrodes were purchased from Metrohm (FL, USA).

2.2 Device design and fabrication

The capillary-driven immunoassay device that automatically delivers reagents for the sandwich ELISA was composed of 5 layers designed in CorelDRAW Graphics suite 2017 as shown in Fig. S1A.† The design layout was cut into PET film, DSA 467MP, and DSA 468MP using a CO_2 laser cutter (Zing 10000, Epilog Laser). These 5 layers were divided into 3 parts as illustrated in Fig. 1A. Part one was attached to parts two and three by foldable hinges. The hinges were created by cutting dashed lines into the PET to make a guideline for folding (Fig. S1†). The detailed composition was as follows: part one was PET film as layer 1, the uppermost layer. This part was used to cover the channels and consisted of a single sample inlet and vent holes. The second part made up the middle part of the device and included layers 2, 3, and 4 which were DSA 468MP, PET film, and DSA 467MP, respectively. The height of the channel is dictated by the height of this middle part. In this part, the channels were cut into 3 pathways that allowed pure sample, detector antibody, or TMB delivery. The path length of each channel was designed to allow sequential delivery of sandwich ELISA reagents. Two channel heights were used throughout the device. The taller channels took longer to fill and contributed to the timing of reagent delivery (cut into layers 2–4 = 0.290 mm of thickness). The shorter channels (cut into layer 2 = 0.130 mm of thickness) took less time to fill and ensured that solution flowed toward the waste pad where the short and tall channels met at the conjugate release pads. All three channels merge into the main channel that is cut in layer 2, which had an arrowhead notch etched in layers 3 and 4 in front of the chamber (the commercial electrode area), followed by an outlet that is connected to a waste pad. This part was fully assembled in the CO_2 laser cutter as previously described.[31] Part three was PET film as layer 5, the bottom layer.

To quantify CRP using the microfluidic device, glass fiber pads were modified to become conjugate-release detector antibody and TMB pads. Following previous studies, the glass fiber was pretreated with 3% w/v sucrose, 0.01% w/v thimerosal, and 0.5% v/v tween 20 in 0.01 M PBS for 15 min at room temperature, then dried overnight at 37 °C.[31,44] The pretreated pads were cut to 3 × 5 mm^2 to fit into the channel. Then, detector antibody pads were dried with 7.5 μL of 1 μg mL^{-1} HRP-labeled anti-CRP antibody in 100 mM Tris-HCl buffer with 0.5% w/v BSA and 0.001% v/v tween 80. The substrate pads were dried with 7.5 μL (×3 times) of commercial TMB solution. To assemble the device, the 3 parts of the capillary-driven immunoassay device were folded as shown in Fig. 1B. The conjugate release detector antibody and TMB pads were installed in the channels prior to sealing the fifth layer. To make the waste pad, Whatman No. 4 filter paper was cut into a fan shape using the laser cutter, where the circular portion had a diameter of 5 cm and was attached to a rectangular channel that inserted into the outlet after assembly (Fig. 1B). Finally, a modified SPCE (screen-printed carbon electrodes) was attached in the slot in layer 1 above the chamber and sealed to the device using the DSA in layer 2 (shown in Fig. S2†) to create an iceCaDI device for CRP measurement. The final iceCaDi device is 5 × 12.6 × 0.5 cm (width × length × height).

2.3 Electrode modification for CRP immunosensor

The commercial SPCEs were electropolymerized to create carboxyl groups on the working electrode (WE) using 20 μL of 7.5 mM PPA in 0.5 M KCl (0–0.85 V, scan rate 0.1 V s^{-1}, 10 cycles).[45] The electrodes were then activated by incubating

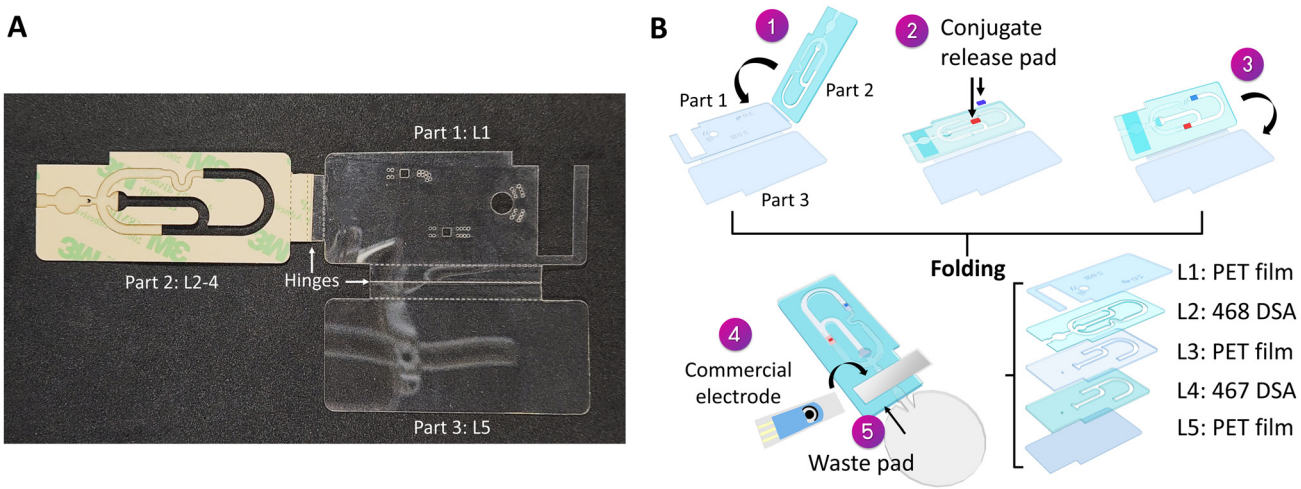

Fig. 1 (A) A photograph of the iceCaDI device before folding. (B) The assembly procedure showing each layer (L).

20 μL of fresh 0.1 M EDC/NHS in 25 mM MES buffer for 30 min. In this work, a streptavidin-biotin system was utilized to immobilize the capture anti-CRP antibody in a more favorable orientation. Therefore, streptavidin was deposited on an activated carboxyl electrode before the biotinylated capture anti-CRP antibody immobilization. The optimal conditions for streptavidin-biotin binding were studied using a biotinylated HRP. As shown in Fig. S3–S5,† the optimal concentrations of substances and incubation times were used as follows: 25 μg mL^{-1} streptavidin incubated for 1 h and 25 μg mL^{-1} biotinylated capture anti-CRP antibody incubated for 15 min. The volume used for each step was 20 μL to cover WE and 200 μL for washing with 25 mM MES buffer (×3 times) after each step. Lastly, a blocking step with 20 μL of 0.5% w/v BSA in 0.01 M PBS was incubated for 30 min to avoid non-specific binding on the electrode surface, followed by washing with 200 μL of 0.01 M PBS (×3 times). All incubation steps were performed in humidity chambers at room temperature (25 °C).

5 mM Ferri/ferrocyanide ($[Fe(CN)_6]^{3-/4-}$) in 0.01 M PBS was used to check for successful electrode modification using cyclic voltammetry (CV) and electrochemical impedance spectroscopy (EIS). The CV measurements were performed at a scan rate of 0.1 V s^{-1} and a potential range of −0.6 V to 0.9 V. For EIS measurements, the potential was applied to 0.16 V with an amplitude of 10 mV in the frequency range 0.01–1 × 10^5 Hz using a PalmSens4 potentiostat (PalmSens BV, Netherlands) at room temperature.

2.4 Procedure for CRP assay and device operation

The iceCaDI device was connected to the portable potentiostat (PalmSens4) and secured in a flat horizontal position. Then, 120 μL of the diluted sample in running buffer (100 mM Tri-HCl buffer) was loaded into the inlet of the device to initiate flow and the sequential delivery of ELISA reagents to the electrodes. Tris-HCl buffer was chosen because it is used commercially for CRP assays. Chronoamperometry was performed with an applied potential of 0.0 V for 480 s to monitor TMB reduction using PSTrance 5.9. Under flow conditions, the chronoamperogram shows an increase in current because the TMB that has been oxidized with the help of the enzyme is reduced at the electrode. The current then decreases, forming a peak, because the plug of oxidized TMB is washed downstream from the electrode over time. For quantification, the three values at the top of the peak were averaged and used to calculate the CRP concentration. The iceCaDI device was discarded after a single use.

3. Results and discussion

3.1 iceCaDI device design strategies

Since the previously designed microfluidic devices for automatically driven sandwich ELISA from our group require skill in aligning and stacking multiple layers,[22,31,46] here, we developed a foldable device that uses hinges for better alignment. There are three parts in the iceCaDI device: the top layer (L1), the middle layers (L2–4), and the bottom layer (L5). The middle and bottom layers are connected with hinges to the top layer (Fig. S1A†). The hinge area of the device is 1 cm in width and contains three cut dashed lines, where the middle line is the hinge that is folded for alignment as shown in Fig. S1.† The dashed line style design was chosen because it is foldable but does not easily tear apart. After the iceCaDI device is folded and stacked as demonstrated in Fig. 1B, the hinge can be torn off using the outer two dashed lines (Fig. 2A). This foldable device design allows for easy multi-layer fabrication and precise alignment, similar to several reports of paper-based devices.[47–49]

Previous eCaDI devices from our group relied on in-house made electrodes.[22,31,46] In this work, an electrode flow cell chamber was incorporated which is the size of commercially available screen-printed electrodes from Metrohm, and has a diameter of 8 mm and a height of 0.13 mm. Fig. 2B demonstrates tunability of the device for applications other than immunosensing because many types of Metrohm SPCE can be incorporated into the device: SPCE, screen printed gold electrodes (SPGE), screen-printed Co(II)-phthalocyanine/carbon electrode, and screen-printed ordered mesoporous carbon/carbon electrode. Each electrode material is suitable for various applications, for example: SPCE is used for immunosensors,[50] screen-printed Co(II)-phthalocyanine/carbon electrode and screen-printed ordered mesoporous carbon/carbon electrode are used for enzymatic sensors,[51,52] and SPGE is used for genosensors.[53]

The fluid in the pump-free laminated device is transported by capillary action and continuous flow is maintained through the absorbent waste pad. However, in complex designs where the fluid comes from both directions in a channel, air bubbles are often trapped in the channel where the fluids meet and cause blockages that stop fluid flow. To address this issue, vent holes (∅ 0.5 mm) in the top layer were added at the junction area where each of the conjugate release pads are installed. Trapped air bubbles were cleared within 27 ± 7 s (Fig. 2C), indicating that the vent holes effectively released the trapped air.

The trapped air bubbles inspired us to use air to our advantage to disperse ELISA reagents coming from the main channel into the wider electrode chamber. In PDMS microchips, arrow-shaped baffles within the microfluidic channel have been proposed to facilitate passive mixing.[54] Due to the generally limited efficacy of laser cutting technology to create a 1 mm-wide barrier in the middle of the stacked laminated channel, we proposed that a purposefully trapped air bubble could act as a baffle. To trap the air bubble, layers 3 and 4 in the middle part of the microfluidic device were perforated in the shape of an arrow with a width of 1 mm in the main channel area just before the electrode chamber. Because of surface tension, the fluid did not flow into the arrow-shaped wedge, causing an air bubble to be trapped. A 3-dimensional model illustrates this concept in Fig. 2D. Fig. 2E demonstrates the dispersion of a 0.5% red dye solution into the running buffer in the electrode chamber after flowing past the arrow-

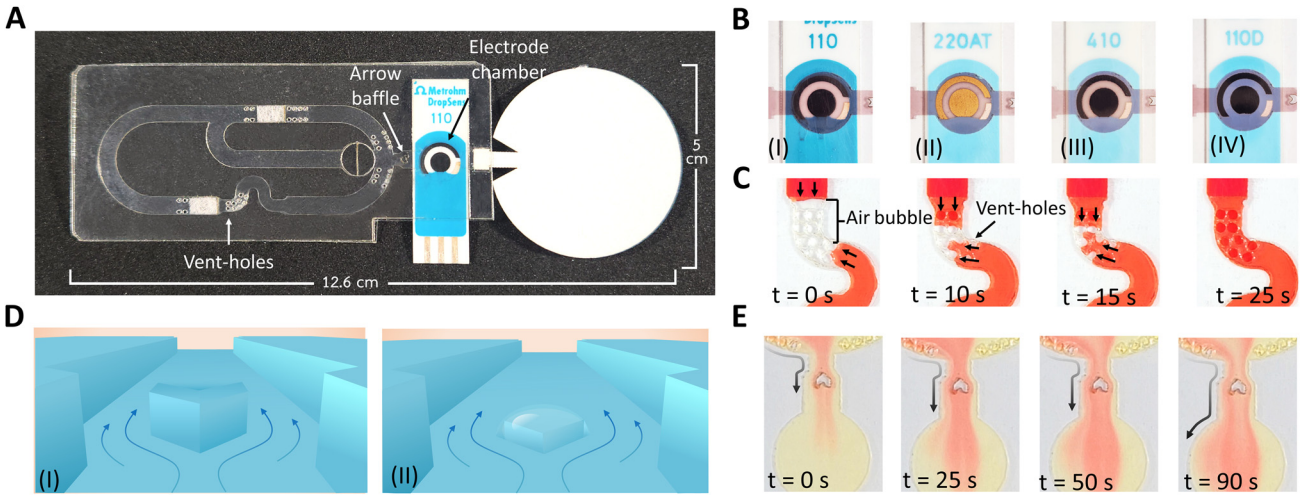

Fig. 2 The iceCaDI device strategy. (A) A photograph of the iceCaDI device after the final assembly. (B) Images of the microfluidic device with various incorporated commercial electrodes: (I) SPCE, (II) screen printed gold electrode (SPGE), (III) screen-printed Co(II)-phthalocyanine/carbon electrode and (IV) screen-printed ordered mesoporous carbon/carbon electrode. (C) Serpentine channel section containing the 9 vent-holes. Images show an air bubble at t = 0 s and its displacement over time using the vent-holes. The direction of flow is denoted by the arrow at t = 0 s. (D) The 3-dimensional model of the arrow-shaped baffle (I) a typical baffle, and (II) the air-formed baffle used in the iceCaDI. (E) Time-lapse images of the trapped air bubble baffle spreading the red-dyed reagent in the electrode chamber. The direction of flow is denoted by the arrow at t = 0 s.

shaped obstacle. In contrast, the absence of the arrow-shaped obstacle results in non-dispersed flow (Fig. S6†). These results demonstrate the successful implementation of a purposefully trapped air bubble that acts as a baffle to promote fluid dispersion in the laminated microfluidic device. It should be noted that these studies were completed with aqueous solutions only, and that solutions with higher viscosities will likely not be dispersed as successfully.

The flow rate in the flow cell in this device design was 0.37 ± 0.04 μL s^{-1}, driven by a waste pad (Whatman No. 4). The optimal volume for this device was 120 μL of running buffer containing the analyte. We found that sample volumes larger than 140 μL caused leakage in the connection area between the fluidic device and the commercial electrodes, because the large volume exceeded the absorbency capacity rate of the waste pad.

3.2 Capture antibody immobilization optimization and modified SPCE characterization

The sandwich ELISA assay was constructed by modifying a capture antibody on the WE and using a detector antibody to form an immunocomplex in which CRP was sandwiched. The SPCE modification is depicted in Fig. 3A. Biotinylated capture antibodies were bound to streptavidin modified on the electrode using PPA and EDC/NHS. For the first optimization steps, the capture antibody was not included in the assay to allow us to characterize device performance without the complete immunoassay. Instead, biotinylated HRP was added to the modified electrode followed by incubation of TMB. Chronoamperometry was then performed, and the average current obtained from each condition was compared. First, the streptavidin immobilization was optimized by comparing different concentrations of streptavidin (Fig. S3†). Although 30 μg mL^{-1} of streptavidin provided the highest amperometric response at 120 s, the current was unstable over time in the chronoamperograms. Therefore, 25 μg mL^{-1} was chosen as the optimal concentration. Next, the blocker (BSA) concentration range was optimized to diminish non-specific binding on the electrodes. BSA was studied in a concentration range of 0.2% to 2% w/v. While all BSA concentrations gave similar signals when streptavidin was not modified on the electrode, the 0.5% w/v of BSA gave the greatest signal change when streptavidin was modified on the electrode, with the smallest standard deviation between trials. Next, the length of time that BSA was incubated on the electrode (blocking time) was studied, using 15 min and 30 min. There was no significant difference between the signals with and without streptavidin for each blocking time, but the 30 min blocking time was selected because there was a lower standard deviation in signal between trials (Fig. S4†). Next, we studied biotin incubation time, and found that the HRP (biotin) was bound to the streptavidin within 10 min; however, we decided to use a 15 min incubation time to reduce operator error (Fig. S5A†). These optimized conditions from the biotinylated HRP were used to identify the optimal capture anti-CRP (biotin) concentration using 10 μg mL^{-1} of CRP and 1 μg mL^{-1} of anti-CRP-HRP in 100 mM Tris-HCl buffer with 0.5% w/v of BSA and 0.001% v/v of tween 80. The current response increased with anti-CRP (biotin) concentration in a dose-dependent manner and then dropped after 25 μg mL^{-1} (Fig. S5B†). This drop in average current can be explained by an excess of biomolecules covering

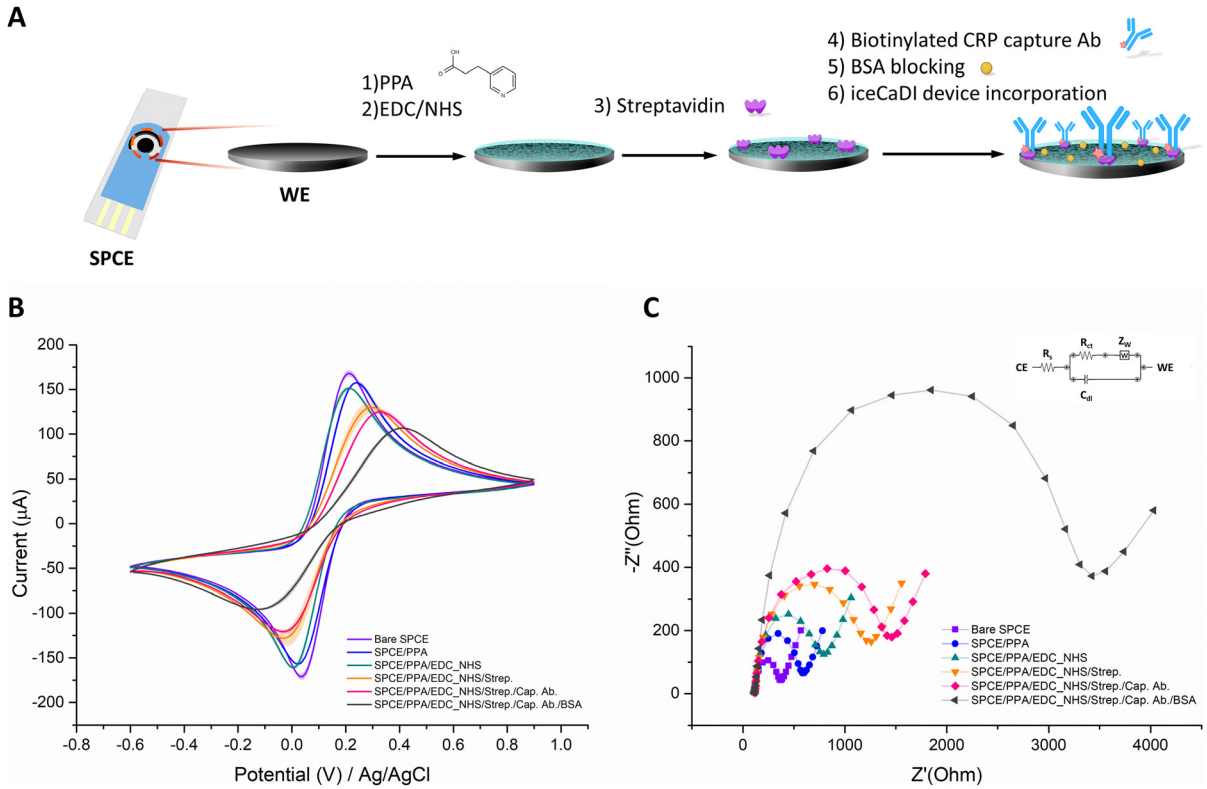

Fig. 3 (A) Overview of electrode preparation for the CRP assay using the iceCaDI device. (B) Cyclic voltammograms and (C) Nyquist plot, results from the investigation of the step-wise electrode modification using 5 mM $[Fe(CN)_6]^{3-/4-}$ in 0.01 M PBS: bare SPCE (purple), the SPCE modified with PPA (blue), the SPCE modified with PPA and EDC/NHS chemistry (green), the SPCE modified with PPA and EDC/NHS chemistry and streptavidin (orange), the SPCE modified with PPA and EDC/NHS chemistry, streptavidin, and the biotinylated capture antibody (red), and the SPCE modified with PPA and EDC/NHS chemistry, streptavidin, the biotinylated capture antibody, and blocked with BSA (black), where the inset in (C) shows the Randles circuit schematic: R_s: the electrolyte resistance, C_{dl}: the double-layer capacitance; R_{ct}: the interfacial charge transfer resistance; Z_w: the Warburg impedance introduced by the diffusion of ions.

the electrodes, which adversely affects the three-dimensional structure of antibodies and the binding of analytes and interrupts charge transfer. Therefore, 25 μg mL^{-1} was chosen as the optimal anti-CRP (biotin) concentration.

The modification of the electrode was monitored after each immobilization step using CV and EIS measurements with 5 mM $[Fe(CN)_6]^{3-/4-}$ in 0.01 M PBS. The cyclic voltammograms had decreased anodic and cathodic peaks (i_p) and increased peak potentials (E_p) as each step of the immobilization procedure was performed (Fig. 3B), which indicates a decrease in electrochemical activity of the electrode due to the additional layers coating the electrode surface. Additionally, the Nyquist plot exhibited an increase in semicircle radius from 270 ± 30 Ω (the bare electrode) to 2.8 ± 0.2 kΩ after the BSA blocking step using the standard Randles equivalent electrical circuit for electrochemical cells (Fig. 3C). The charge transfer resistance (R_{ct}), calculated by the diameter of the semi-circle in the Nyquist plot, increased as each layer of the immunoassay was modified on the electrode surface because the molecules coating the electrodes are insulating, hindering electron transfer. These results confirmed the success of anti-CRP immobilization.

3.3 Flow studies and sequential delivery of reagents

In accordance with the sandwich ELISA assay, the iceCaDI device was designed to consist of 3 channels, labeled in Fig. 4A, where channel 1 first delivers the sample containing the analyte, CRP, to the capture antibody modified WE. Next, channel 2 delivers the detector antibody, followed by delivery of TMB from channel 3. Sequential delivery of the reagents was achieved by tailoring the channel length, width, and height to manipulate the time that the reagents were delivered to the WE.

Simple laminated devices with a single 4 cm-long channel and a channel height of 0.29 mm were created to study fluid flow. Two channel conditions were fabricated, with either a 2 mm or 3 mm wide channel. Flow studies were performed to optimize reagent delivery using 150 μL of 0.5% food dye in running buffer. Velocity was measured from video recordings based on the time required for the fluid front to flow over each 1 cm distance. We found that both the 2- and 3 mm width channels showed a decreasing velocity from a 1 cm distance from the inlet to 4 cm, with velocities of 11 ± 5 to 2.3 ± 0.3 cm s^{-1} and 6.3 ± 0.8 to 2.2 ± 0.3 cm s^{-1}, respectively. As the dis-

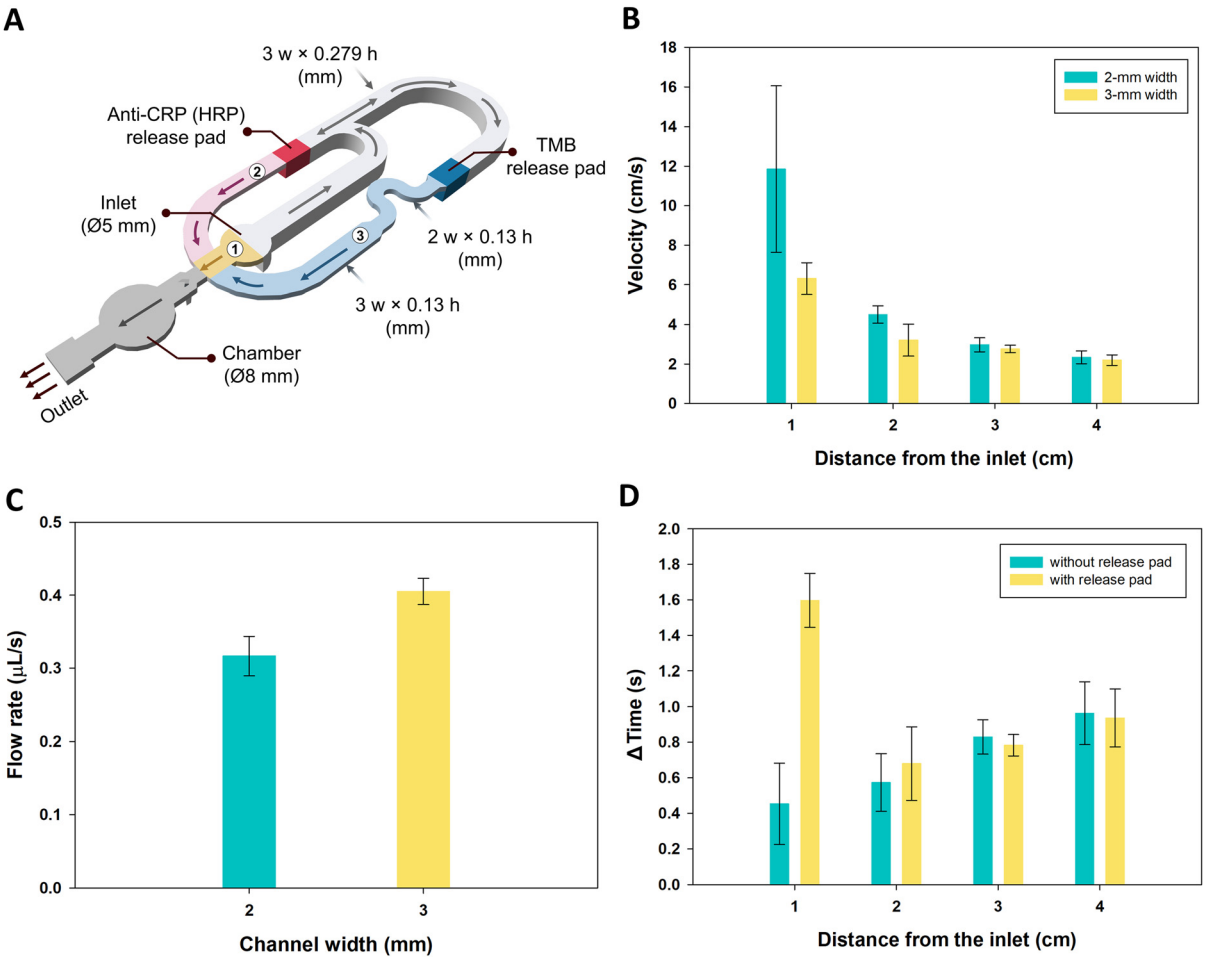

Fig. 4 Flow studies for the iceCaDI. (A) A three-dimensional view of the iceCaDI channels. (B) A comparison of the velocity in simple microfluidic channels with 2- or 3 mm widths and a 4 cm channel length. The velocity is measured at 1 cm increments from the inlet. (C) The measured volumetric flow rate in the same devices as B. (D) The time required for solution to flow in 3 mm wide and 4 cm long channels with and without the installed conjugate release pad; ΔTime represents the amount of time required for the fluid front to cross each 1 cm distance from the conjugated release pad.

tance from the inlet increased, the velocity decreased due to the pressure drop along the length of the channel (Fig. 4B). The flow velocity changes once it is driven by the waste pad. To measure the flow velocity driven by the waste pad, similar experiments were performed as those described for Fig. 4B, except instead of measuring the fluid front velocity, the trailing air bubble velocity was measured. The flow velocity was driven by the waste pad at 0.36 ± 0.01 mm s^{-1} (Fig. S7A†) after the liquid was fully loaded. The flow rate of the waste pad was measured by dividing the total sample volume added by the amount of time required to wick the sample from the inlet fully into the waste pad (Fig. S7B†). As expected, based on the pore size of the paper, Whatman No. 4 filter paper had a higher flow rate than Whatman No. 1 filter paper (0.160 ± 0.003 μL s^{-1}). Therefore, we used Whatman No. 4 as the waste pad (Fig. S7B†). Although the 2 mm width channel had a greater velocity than the 3 mm width channel, the volumetric flow rate (measured the same as the experiments in Fig. S7B†) of the 2 mm width channel (0.32 ± 0.03 μL s^{-1}) was lower than that of the 3 mm width channel (0.41 ± 0.02 μL s^{-1}), as shown in Fig. 4B and C. The pressure drop and impact of the cross-sectional area of the channel to flow behaviour agrees with friction factor and Bernoulli's principle, respectively.[55] Since the TMB from the substrate pad must be transported to the WE last, a serpentine channel with a width of 2 mm was added between the substrate pad and the WE to slow down the volumetric flow rate and increase the path length. When a conjugate release pad was installed in the channel, the flow was attenuated because of the time needed to rehydrate the pad. The time required for the solution to reach 1 cm past the conjugate pad location went from 0.5 ± 0.2 s to 1.6 ± 0.2 s, as shown in Fig. 4D. However, the velocity quickly recovered. Additionally, we found that the flow in the laminated channels was >10 times faster than the flow in nitrocellulose membranes (Fig. S8†).

Fig. 5A demonstrates the concept of CRP sandwich ELISA detection by chronoamperometry. Here, food dye (0.5%) in running buffer was used to demonstrate the sequential flow of

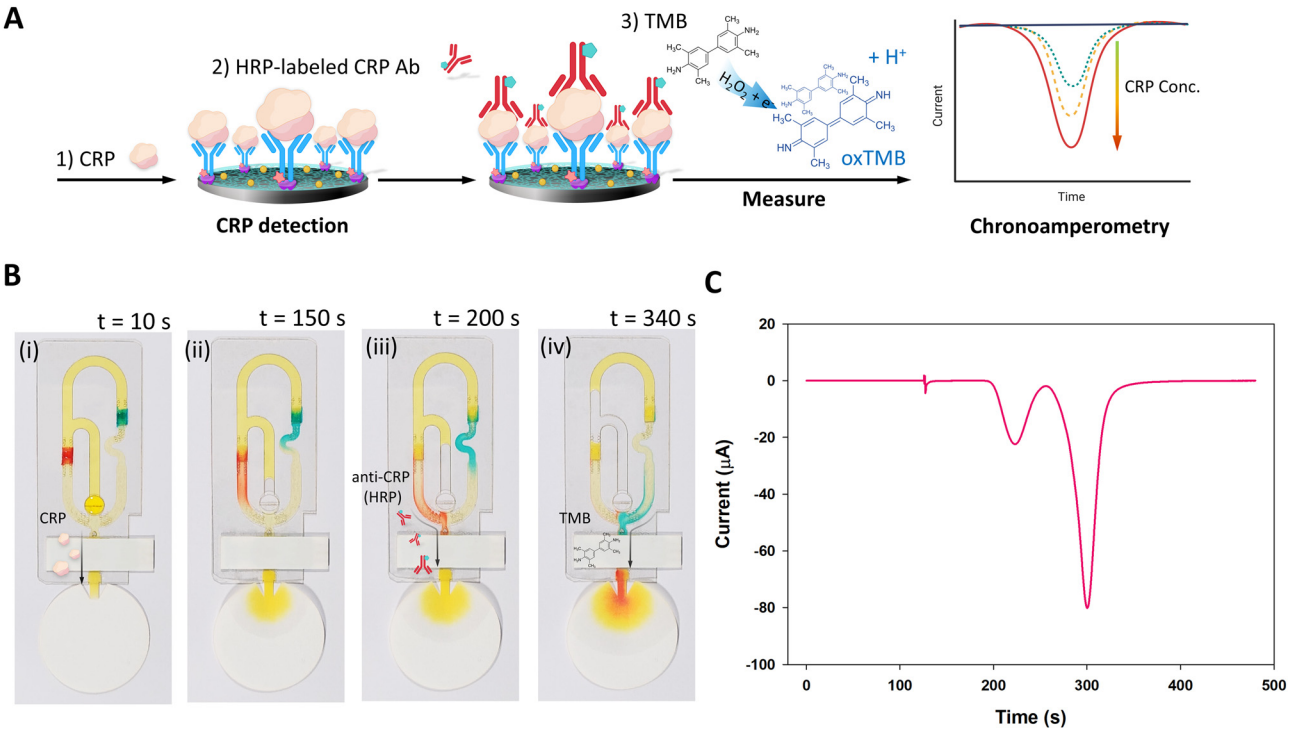

Fig. 5 (A) Overview of electrochemical detection for the CRP assay using the iceCaDI device. (B) Images of the device with 0.5% yellow food dye in running buffer, to demonstrate sequential delivery of the target to the SPCE (i), the inlet emptying and the channels filling with air (ii), delivery of the detector antibody (represented by red food dye) to the electrode (iii), and delivery of the TMB (represented by blue food dye) to the electrode. (C) A chronoamperogram was collected using the iceCaDI where the two conjugated pads were treated with 7.5 μL or 15 μL of 5 mM $[Fe(CN)_6]^{3-/4-}$ for the detector antibody and TMB pads, respectively.

the sandwich ELISA reagents, shown in Fig. 5B. Yellow food dye solution (120 μL) represents a sample solution containing CRP, the target of the assay. After loading into the sample inlet, the yellow solution fills the channels (Fig. 5B part (i)) and immediately flows across the modified commercial SPCE towards the waste pad. The WE of the SPCE is modified with capture antibodies for CRP, so the target binds to the electrode. Meanwhile, the yellow solution fills the channels on both sides of the conjugate release pads (Fig. 5B part (ii)). The path to the pad that has been treated with red dye, representing the detector antibody, is shortest, so it is delivered to SPCE next. The red dye arrived at the SPCE chamber at 170 ± 10 s after sample delivery, which represents the detector antibodies forming a sandwich complex on the WE (Fig. 5B part (iii)). As the solution continues being pulled from the sample inlet through the channels towards the waste pad, the channels fill with air, which acts as a barrier that stops flow. Last, the blue dye, which represents the substrate, TMB, arrived at the SPCE chamber at 310 ± 50 s. TMB oxidation is catalyzed by the HRP on the immunocomplex and is subsequently reduced by performing chronoamperometry to evaluate the concentration of the target.

To confirm the flow time and reagent release from the conjugate release pads, an electroactive molecule was dried on the conjugate release pads: 7.5 μL of 5 mM $[Fe(CN)_6]^{3-/4-}$ on the detector antibody pad and 15 μL of 5 mM $[Fe(CN)_6]^{3-/4-}$ on the TMB pad. Subsequently, 120 μL of running buffer was added to the sample inlet and chronoamperometry was performed to observe the current, shown in Fig. 5C. The first and smaller peak response (−23 μA) corresponds to the delivery of reagents from the detector antibody pad, which occurred at 224 ± 1 s. The second and larger peak response corresponds to delivery of reagents from the TMB pad at 300 ± 1 s. The current returned to baseline between the two peaks, demonstrating that the two reagents are delivered sequentially, not simultaneously. This feature is important because it is undesirable for the TMB to mix with HRP-labelled antibodies that are not bound to the immunocomplex on the WE, so that the measured current accurately reflects the target concentration. The total time required to obtain the two peak current measurements for this design was 410 ± 70 s. Therefore, 480 s was chosen as the length of time to perform chronoamperometry for assay measurements. Alternatively, the measurement could be completed after the peak of the current response appeared.

3.4 Application of the iceCaDI device for a CRP assay

The dose–response of the developed CRP immunosensor was evaluated with seven concentrations of CRP standards (0 to 40 μg mL^{-1}) using three independent electrode measurements under static conditions, shown in Fig. 6A. The concentrations of CRP (μg mL^{-1}) and the current response (Δcurrent; target

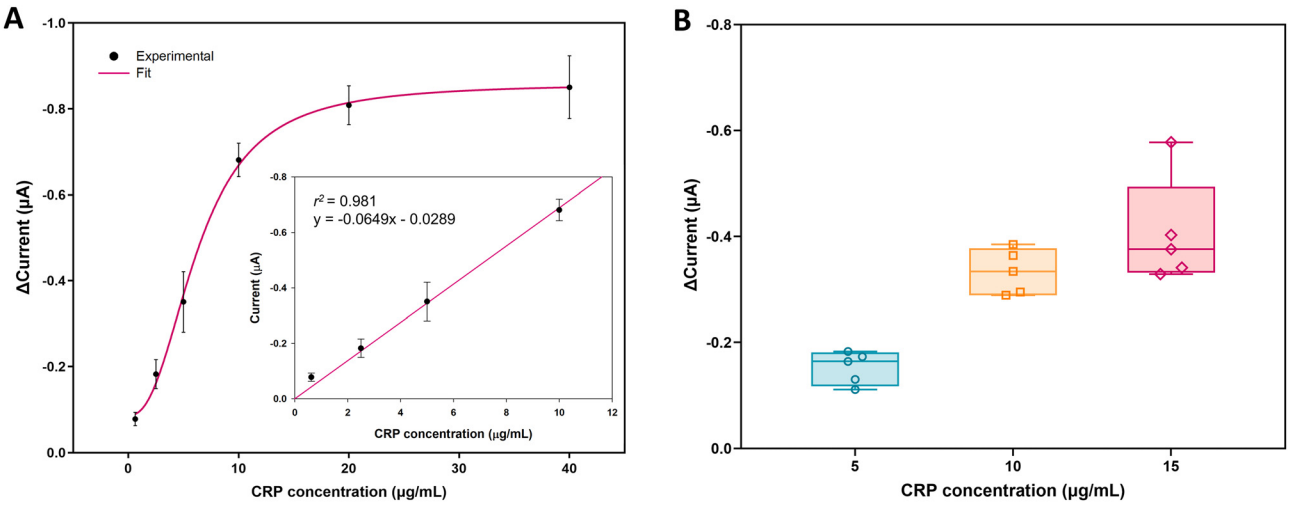

Fig. 6 The dose–response curve of CRP obtained by chronoamperometry. (A) Results from the static CRP immunosensor. The inset shows the corresponding calibration curve plotted for the CRP concentrations from 0.625 to 10.0 μg mL^{-1} (r^2 = 0.981); Δcurrent = target signal – blank signal. (B) Results obtained using several CRP concentrations in the iceCaDI device.

signal – blank signal) were plotted to construct a calibration curve. The plot showed an increase in current with increasing CRP concentration. A static linear range of 0.625 to 10.0 μg mL^{-1} for CRP was obtained with a correlation coefficient (r^2) of 0.981 (inset, Fig. 6A). This calibration curve provided a linear response of (Δcurrent) = [−0.0649 × CRP concentration (μg mL^{-1})] − 0.0289 for the CRP assay. Moreover, the limit of detection (LOD) and limit of quantitation (LOQ), which were calculated using three times and 10 times the standard deviation of the blank signal divided by the slope of the linear portion of the calibration curve, were 0.751 and 2.277 μg mL^{-1}, respectively. The average normal serum level of CRP is 0.8 μg mL^{-1} in healthy humans;[56] moreover, the American Heart Association (AHA) and the United States Center for Disease Control (CDC) divide the concentration of high-sensitivity CRP (hs-CRP) into three levels: <1, 1–3, and 3–10 μg mL^{-1}, where each range is associated with a low, moderate, or high risk of cardiovascular disease (CVD) progression, respectively, where all are within the linear range of this CRP immunosensor.[57,58] Thus, the proposed CRP immunosensor shows the potential to detect CRP at clinically relevant levels. However, the CRP concentration can be significantly elevated up to 1000-fold over the normal level in case of inflammation.[39] This high CRP concentration is outside of the linear range of the proposed immunosensor, so the sample would need to be diluted to avoid the hook effect.[59]

Finally, the CRP immunosensor was deployed in the iceCaDI device to demonstrate its automated sequential sandwich ELISA reagent delivery. Since the clinical cut-off value for CRP in human serum is ≥10 μg mL^{-1} (~87 nM),[60] three concentrations close to 10 μg mL^{-1} CRP were evaluated in the iceCaDI. In-flow electrochemical detection revealed peak current responses of −0.15 ± 0.03, −0.33 ± 0.04, and −0.4 ± 0.1 μA for 5.00, 10.0, and 15.0 μg mL^{-1} of CRP, respectively (Fig. 6B). Each concentration was tested with five different iceCaDI devices. The results demonstrated an increase in peak current with an increase in CRP concentration, which illustrates the successful performance of the iceCaDI device for single-step sandwich ELISA assays. For clinical implementation of CRP quantification, dilution of the sample may be necessary to mitigate the hook effect and reduce sample matrix interference, which may decrease the sensitivity of this device.

4. Conclusions

In this work, we successfully developed a pump-free, portable, capillary-driven immunoassay device for electrochemical detection with a flow rate of 0.37 ± 0.04 μL s^{-1} driven by a waste pad (Whatman No. 4 filter paper). An integrated commercial electrode chamber size was standardized to 8 mm diameter and 0.13 mm height and was compatible with a wide range of commercial electrodes. Our incorporated commercial electrode into a capillary-driven immunoassay (iceCaDI) device automatically performed sequential delivery of sandwich ELISA reagents as a single-use test. The iceCaDI device consisted of three layers of PET film, and two layers of DSA film that were patterned using a laser cutter. We developed a foldable laminated device using dashed lines to guide the fold and act as a hinge for precise alignment. The hinges were employed to connect three layers of the PET film with the DSA film inserted between them for easy assembly. Next, vent-holes (⌀ 0.5 mm) were added to the device design to allow trapped air bubbles to escape. Additionally, we introduced a 1 mm arrow-shaped baffle in the middle of the laminated channel to improve dispersal of reagents. An arrow-shaped notch was cut in the bottom of the channel, which trapped an air bubble that formed a baffle. The arrow-shaped baffle was added in the main channel before the flow cell, allowing the reagents to dis-

perse and cover the entire detection area (working electrode). All flow phenomena of the iceCaDI device were examined including the effects of flow rate, velocity, and addition of a conjugate release pads. Lastly, to demonstrate the applicability of the iceCaDI, we created a CRP immunosensor with a static linear range of 0.625 to 10.0 μg mL^{-1} (limit of detection = 0.751 μg mL^{-1}). Three clinical CRP concentrations were successfully measured in the iceCaDI device to demonstrate the single end-user step sandwich ELISA for CRP quantification within 8 minutes. This platform and these design features offer great potential for electrochemical applications which can be extended to other biomarkers that have been commonly utilized in a traditional sandwich ELISA to serve as a simple, low-cost, disposable, and portable quantitative POC test for decentralized laboratories in the future.

Author contributions

Phuritat Kaewarsa: Conceptualization, methodology, formal analysis, investigation, writing – original draft, visualization. Melissa S. Schenkel: Conceptualization, methodology. Kira L. Rahn: Writing – review & editing. Wanida Laiwattanapaisal: Supervision. Charles S. Henry: Conceptualization, methodology, resources, writing – review & editing, project administration, funding acquisition.

Conflicts of interest

There are no conflicts to declare.

Acknowledgements

P. K. gratefully acknowledges the financial support from the National Research Council of Thailand (NRCT) in the Royal Golden Jubilee Ph.D. Program (Grant No. PHD/0058/2560). P. K. would like to thank the Henry Group for all their support at Colorado State University. This work was also supported by a grant from the National Institutes of Health to CSH (R01EB031510).

References

1 P. Ferrer, C. Bastias, C. Beltrán and A. Afani, *J. Clin. Virol. Plus*, 2022, **2**, 100064.
2 C. V. Eley, A. Sharma, D. M. Lecky, H. Lee and C. A. M. McNulty, *BMJ Open*, 2018, **8**, e023925.
3 F. Boscari, S. Galasso, A. Facchinetti, M. C. Marescotti, V. Vallone, A. M. L. Amato, A. Avogaro and D. Bruttomesso, *Nutr., Metab. Cardiovasc. Dis.*, 2018, **28**, 180–186.
4 J. H. Nichols, in *Contemporary Practice in Clinical Chemistry (Fourth Edition)*, ed. W. Clarke and M. A. Marzinke, Academic Press, 2020, pp. 323–336.
5 J. A. Otoo and T. S. Schlappi, *Biosensors*, 2022, **12**, 124.
6 C. S. Kosack, A. L. Page and P. R. Klatser, *Bull. W. H. O.*, 2017, **95**, 639–645.
7 Y. Wu, Y. Zhou, Y. Leng, W. Lai, X. Huang and Y. Xiong, *Biosens. Bioelectron.*, 2020, **157**, 112168.
8 O. Filchakova, D. Dossym, A. Ilyas, T. Kuanysheva, A. Abdizhamil and R. Bukasov, *Talanta*, 2022, **244**, 123409.
9 C. Gnoth and S. Johnson, *Geburtshilfe Frauenheilkd.*, 2014, **74**, 661–669.
10 Q. Zhang, L. Fang, B. Jia, N. Long, L. Shi, L. Zhou, H. Zhao and W. Kong, *TrAC, Trends Anal. Chem.*, 2021, **144**, 116427.
11 C. Zhang, Y. Zhang and S. Wang, *J. Agric. Food Chem.*, 2006, **54**, 2502–2507.
12 J.-H. Cho, E.-H. Paek, I.-H. Cho and S.-H. Paek, *Anal. Chem.*, 2005, **77**, 4091–4097.
13 A. Kawde, X. Mao, H. Xu, Q. Zeng, Y. He and G. Liu, *Am. J. Biomed. Sci.*, 2010, 23–32.
14 K. V. Serebrennikova, N. A. Byzova, A. V. Zherdev, N. G. Khlebtsov, B. N. Khlebtsov, S. F. Biketov and B. B. Dzantiev, *Biosensors*, 2021, **11**, 510.
15 M. P. Nguyen, N. A. Meredith, S. P. Kelly and C. S. Henry, *Anal. Chim. Acta*, 2018, **1017**, 20–25.
16 J. Budd, B. S. Miller, N. E. Weckman, D. Cherkaoui, D. Huang, A. T. Decruz, N. Fongwen, G.-R. Han, M. Broto, C. S. Estcourt, J. Gibbs, D. Pillay, P. Sonnenberg, R. Meurant, M. R. Thomas, N. Keegan, M. M. Stevens, E. Nastouli, E. J. Topol, A. M. Johnson, M. Shahmanesh, A. Ozcan, J. J. Collins, M. F. Suarez, B. Rodriguez, R. W. Peeling and R. A. McKendry, *Nat. Rev. Bioeng.*, 2023, **1**, 13–31.
17 B. A. Baldo, E. R. Tovey and S. A. Ford, *J. Biochem. Biophys. Methods*, 1986, **12**, 271–279.
18 K. Omidfar, F. Riahi and S. Kashanian, *Biosensors*, 2023, **13**, 837.
19 J. Songok and M. Toivakka, *Microfluid. Nanofluid.*, 2016, **20**, 63.
20 M. Liu, J. Wu, Y. Gan, D. A. H. Hanaor and C. Q. Chen, *Langmuir*, 2016, **32**, 9899–9904.
21 S. Chang, J. Seo, S. Hong, D.-G. Lee and W. Kim, *J. Fluid Mech.*, 2018, **845**, 36–50.
22 I. C. Samper, A. Sánchez-Cano, W. Khamcharoen, I. Jang, W. Siangproh, E. Baldrich, B. J. Geiss, D. S. Dandy and C. S. Henry, *ACS Sens.*, 2021, **6**, 4067–4075.
23 J. S. Link, C. S. Carrell, I. Jang, E. J. O. Barstis, Z. D. Call, R. A. Bellows, J. J. O'Donnell-Sloan, J. S. Terry, L. B. R. Anderson, Y. Panraksa, B. J. Geiss, D. S. Dandy and C. S. Henry, *Anal. Chim. Acta*, 2023, **1277**, 341634.
24 N. S. Moreira, C. L. S. Chagas, K. A. Oliveira, G. F. Duarte-Junior, F. R. de Souza, M. Santhiago, C. D. Garcia, L. T. Kubota and W. K. T. Coltro, *Anal. Chim. Acta*, 2020, **1119**, 1–10.
25 P. Lakhera, V. Chaudhary, B. Bhardwaj, P. Kumar and S. Kumar, *Biosens. Bioelectron.: X*, 2022, **11**, 100218.
26 S. Chen, Z. Wang, X. Cui, L. Jiang, Y. Zhi, X. Ding, Z. Nie, P. Zhou and D. Cui, *Nanoscale Res. Lett.*, 2019, **14**, 71.

27 G. Ebrahimi, P. S. Pakchin, A. Shamloo, A. Mota, M. de la Guardia, H. Omidian and Y. Omidi, *Microchim. Acta*, 2022, **189**, 252.
28 S. Ramalingam, A. Elsayed and A. Singh, *Microchim. Acta*, 2020, **187**, 645.
29 P. K. Kalambate, P. Thirabowonkitphithan, P. Kaewarsa, K. Permpoka, A. B. Radwan, R. A. Shakoor, R. P. Kalambate, H. Khosropour, Y. Huang and W. Laiwattanapaisal, *Mater. Today Chem.*, 2022, **26**, 101235.
30 M. Negahdary, W. A. Ameku, B. G. Santos, I. dos Santos Lima, T. Gomes de Oliveira, M. C. França and L. Angnes, *Microchem. J.*, 2023, **185**, 108281.
31 K. M. Clark, M. S. Schenkel, T. W. Pittman, I. C. Samper, L. B. R. Anderson, W. Khamcharoen, S. Elmegerhi, R. Perera, W. Siangproh, A. J. Kennan, B. J. Geiss, D. S. Dandy and C. S. Henry, *ACS Meas. Sci. Au*, 2022, **2**, 584–594.
32 Q. Cao, B. Liang, T. Tu, J. Wei, L. Fang and X. Ye, *RSC Adv.*, 2019, **9**, 5674–5681.
33 G. Lee, J. Lee, J. Kim, H. S. Choi, J. Kim, S. Lee and H. Lee, *Sci. Rep.*, 2017, **7**, 7545.
34 E. L. Fava, T. A. Silva, T. M. d. Prado, F. C. d. Moraes, R. C. Faria and O. Fatibello-Filho, *Talanta*, 2019, **203**, 280–286.
35 L.-L. Ma, Y. He, D. Qin, A. Chang, A. Huang, X.-J. Xie and Y. Zheng, *Chin. J. Anal. Chem.*, 2021, **49**, e21187–e21196.
36 P. Fanjul-Bolado, D. Hernández-Santos, P. J. Lamas-Ardisana, A. Martín-Pernía and A. Costa-García, *Electrochim. Acta*, 2008, **53**, 3635–3642.
37 N. Serrano, Ò. Castilla, C. Ariño, M. S. Diaz-Cruz and J. M. Díaz-Cruz, *Sensors*, 2019, **19**, 4039.
38 B. Clyne and J. S. Olshaker, *J. Emerg. Med.*, 1999, **17**, 1019–1025.
39 W. Ansar and S. Ghosh, *Immunol. Res.*, 2013, **56**, 131–142.
40 W. S. Tillett and T. Francis, *J. Exp. Med.*, 1930, **52**, 561–571.
41 T. Songjaroen, R. M. Feeny, M. M. Mensack, W. Laiwattanapaisal and C. S. Henry, *Sens. Bio-Sens. Res.*, 2016, **8**, 14–19.
42 R. Wu, S. Zhou, T. Chen, J. Li, H. Shen, Y. Chai and L. S. Li, *Anal. Chim. Acta*, 2018, **1008**, 1–7.
43 Y. Cai, K. Kang, Y. Liu, Y. Wang and X. He, *Anal. Biochem.*, 2018, **556**, 129–135.
44 B. D. Grant, C. E. Anderson, J. R. Williford, L. F. Alonzo, V. A. Glukhova, D. S. Boyle, B. H. Weigl and K. P. Nichols, *Anal. Chem.*, 2020, **92**, 11305–11309.
45 V. Primpray, W. Kamsong, S. Pakapongpan, K. Phochakum, A. Kaewchaem, A. Sappat, A. Wisitsoraat, T. Lomas, A. Tuantranont and C. Karuwan, *Talanta Open*, 2022, **6**, 100155.
46 T. Sierra, C. S. Henry, A. G. Crevillén and A. Escarpa, *Anal. Sens.*, 2022, **2**, e202100038.
47 P. Kaewarsa, T. Vilaivan and W. Laiwattanapaisal, *Anal. Chim. Acta*, 2021, **1186**, 339130.
48 S. Boonkaew, S. Chaiyo, S. Jampasa, S. Rengpipat, W. Siangproh and O. Chailapakul, *Microchim. Acta*, 2019, **186**, 153.
49 C.-A. Chen, W.-S. Yeh, T.-T. Tsai, Y.-D. Li and C.-F. Chen, *Lab Chip*, 2019, **19**, 598–607.
50 A. Valverde, V. Serafín, A. Montero-Calle, A. González-Cortés, R. Barderas, P. Yáñez-Sedeño, S. Campuzano and J. M. Pingarrón, *ChemElectroChem*, 2020, **7**, 810–820.
51 A. Miar, D. Hevia, H. Muñoz-Cimadevilla, A. Astudillo, J. Velasco, R. M. Sainz and J. C. Mayo, *Free Radicals Biol. Med.*, 2015, **85**, 45–55.
52 R. Zumpano, L. Lambertini, C. Tortolini, P. Bollella, G. Favero, R. Antiochia and F. Mazzei, *J. Power Sources*, 2020, **476**, 228615.
53 Ravina, A. Dalal, P. S. Gill, J. Narang, M. Prasad and H. Mohan, *Process Biochem.*, 2020, **98**, 262–268.
54 T. Songjaroen, T. Maturos, A. Sappat, A. Tuantranont and W. Laiwattanapaisal, *Anal. Chim. Acta*, 2009, **647**, 78–83.
55 G. Barker, in *The Engineer's Guide to Plant Layout and Piping Design for the Oil and Gas Industries*, ed. G. Barker, Gulf Professional Publishing, 2018, pp. 411–472.
56 K. Dhara and D. R. Mahapatra, *Microchem. J.*, 2020, **156**, 104857.
57 J. P. Araújo, P. Lourenço, A. Azevedo, F. Friões, F. Rocha-Gonçalves, A. Ferreira and P. Bettencourt, *J. Card. Failure*, 2009, **15**, 256–266.
58 J. J. Carrero, M. A. Franko, A. Obergfell, A. Gabrielsen and T. Jernberg, *J. Am. Heart Assoc.*, 2019, **8**, e012638.
59 S. K. Vashist and J. H. T. Luong, in *Handbook of Immunoassay Technologies*, ed. S. K. Vashist and J. H. T. Luong, Academic Press, 2018, pp. 81–95.
60 S. Black, I. Kushner and D. Samols, *J. Biol. Chem.*, 2004, **279**, 48487–48490.